Monthly Notices of the ROYAL ASTRONOMICAL SOCIETY

MNRAS **496,** 125–137 (2020)
Advance Access publication 2020 May 30

doi:10.1093/mnras/staa1464

67P/Churyumov–Gerasimenko's dust activity from pre- to post-perihelion as detected by *Rosetta*/GIADA

A. Longobardo,[1]★ V. Della Corte,[1] A. Rotundi,[1,2] M. Fulle,[3] G. Rinaldi,[1] M. Formisano,[1] V. Zakharov,[1] S. Ivanovski,[3] T. Mannel,[4] M. Ciarniello,[1] L. Inno,[2] M. Rubin,[5] E. Palomba,[1,6] H. Cottin,[7] F. Dirri,[1] P. Palumbo,[1,2] C. Güttler,[8] S. Merouane,[8] C. Tubiana,[8] B. Pestoni[5] and Z. Dionnet[2]

[1]*INAF-IAPS, via Fosso del Cavaliere 100, I-00133 Rome, Italy*
[2]*Università di Napoli 'Parthenope', DIST, Centro Direzionale Isola C4, I-80143 Naples, Italy*
[3]*INAF-OATS, via G.B. Tiepolo 11, I-34143 Trieste, Italy*
[4]*Space Research Institute of the Austrian Academy of Sciences, A-8042 Graz, Austria*
[5]*Physikalisches Institut, University of Bern, CH-3012 Bern, Switzerland*
[6]*ASI-SSDC, via del Politecnico snc, I-00133 Rome, Italy*
[7]*LISA, UMR CNRS 7583, Université Paris-Est-Créteil, Université de Paris, Institut Pierre Simon Laplace (IPSL), F-94010 Créteil, France*
[8]*Max Planck Institute, D-37077 Göttingen, Germany*

Accepted 2020 May 19. Received 2020 May 19; in original form 2020 April 2

ABSTRACT

We characterized the 67P/Churyumov–Gerasimenko's dust activity, by analysing individual dust particle velocity and momentum measurements of Grain Impact Analyser and Dust Accumulator (GIADA), the dust detector onboard the ESA/*Rosetta* spacecraft, collecting dust from tens to hundreds of kilometres from the nucleus. Specifically, we developed a procedure to trace back the motion of dust particles down to the nucleus, identifying the surface's region ejecting each dust particle. This procedure has been developed and validated for the first part of the mission by Longobardo et al. and was extended to the entire GIADA data set in this work. The results based on this technique allowed us to investigate the link between the dust porosity (fluffy/compact) and the morphology of the ejecting surface (rough/smooth). We found that fluffy and compact particles, despite the lack of correlation in their coma spatial distribution (at large nucleocentric distances) induced by their different velocities, have common ejection regions. In particular, the correlation between the distributions of fluffy and compact particles is maintained up to an altitude of about 10 km. Fluffy particles are more abundant in rough terrains. This could be the result of past cometary activity that resurfaced the smooth terrains and/or of the comet formation process that stored the fluffy particles inside the voids between the pebbles. The variation of fluffy particle concentration between rough and smooth terrains agrees with predictions of comet formation models. Finally, no correlation between dust distribution on the nucleus and surface thermal properties was found.

Key words: instrumentation: detectors – methods: data analysis – comets: individual: Churyumov–Gerasimenko.

1 INTRODUCTION

The ESA/*Rosetta* mission orbited comet 67P/Churyumov–Gerasimenko from 2014 August to 2016 September. The *Rosetta* spacecraft escorted the comet and observed different stages of its orbit including its perihelion passage (2015 August 13). Before perihelion, 67P was poorly active and its surface properties were mostly influenced by processes that occurred during previous perihelion passages and modifications far from the Sun (e.g. by space weathering). While the comet approached the Sun, its activity led to rejuvenation of its surface, exposing underlying and more pristine material. After perihelion, nucleus surface and coma were partially renewed by the occurred activity.

67P's nucleus is bilobate shaped and characterized by a head, a body, and a neck connecting them (Sierks et al. 2015). The Optical, Spectroscopic, and Infrared Remote Imaging System (OSIRIS) camera (Keller et al. 2007) identified geological and

★ E-mail: andrea.longobardo@inaf.it

© 2020 The Author(s)
Published by Oxford University Press on behalf of the Royal Astronomical Society

Downloaded from https://academic.oup.com/mnras/article/496/1/125/5849013 by guest on 31 January 2025

geomorphological regions on the nucleus surface by observing the Northern hemisphere before perihelion (El-Maarry et al. 2015) and the Southern hemisphere in the post-perihelion stage (El-Maarry et al. 2016). The composition of the nucleus surface, as inferred by the Visible and Infrared Thermal Imaging Spectrometer (VIRTIS) imaging spectrometer (Coradini et al. 2007), is a mixture of opaque minerals, organics (Capaccioni et al. 2015; Raponi et al. 2020), ammonium salts (Poch et al. 2020), and water ice (Barucci et al. 2016; Filacchione et al. 2016; Raponi et al. 2016). The amount of water ice on the surface has a diurnal and seasonal variation (De Sanctis et al. 2015; Ciarniello et al. 2016).

Coma observations have revealed that dust and water vapour emissions are correlated spatially (Rinaldi et al. 2016), but not temporally (Tubiana et al. 2019), at least during the pre-perihelion stage. Outbursts, i.e. sudden increase of the dust emission, have been observed during the entire mission: some of them showed a change of the dust colour from red to blue, revealing the presence of very small grains ($\leq$100 nm; Bockelée-Morvan et al. 2017).

In situ measurements of the Grain Impact Analyser and Dust Accumulator (GIADA) instrument (Della Corte et al. 2014) detected mm-sized dust particles, belonging to two different porosity groups (Fulle et al. 2015; Rotundi et al. 2015), i.e. compact (0.03–1 mm in size) and fluffy particles (0.2–2.5 mm in size), as well as accumulation of μm- and nm-sized dust particles (Della Corte et al. 2019). Cometary dust can generally be classified in three groups characterized by their porosity (Güttler et al. 2019): solid (porosity $<$ 10 per cent), porous (porosity between 10 and 95 per cent), and fluffy (porosity $>$ 95 per cent). Because GIADA was not able to discern solid and porous particles, we group the two families under the name 'compact'. Fluffy particles detected by GIADA were fragments of single pristine fluffy agglomerates, broken by the spacecraft electrostatic potential (Fulle et al. 2015), and represent the most pristine particles from the protoplanetary nebula (Fulle & Blum 2017). Even if fluffy and compact particles do not spatially correlate in the coma, it has been found that, at least in the first part of the pre-perihelion stage, they were generated from the same nucleus sources and then were spread in the coma due to their different speeds (Longobardo et al. 2019a): the dust activity maps obtained for this period are archived on PDA/PDS (Rotundi & the International GIADA Consortium 2019). Moreover, the combination of GIADA and VIRTIS data has shown that in this stage of the orbit a stronger dust emission is associated with a larger exposition of water ice from the subsurface (Longobardo et al. 2019a).

The aim of this work is twofold. (1) Mapping the dust activity of the comet, by defining the origin and distribution of fluffy and compact dust particles in different orbital stages. In order to achieve this goal, we traced back the motion of all the dust particles detected by GIADA during the entire *Rosetta* mission by extending the procedure we already developed and validated for the first part of the mission. (2) Investigating the role of cometary activity at different spatial scales, by probing a possible relation between the dust particles morphology and the surface geomorphology of the ejecting regions. In both cases we could obtain different results depending on the mission phases, because of the possible seasonal changes of dust properties (Fulle et al. 2016; Merouane et al. 2017).

We describe data in Section 2 and the traceback procedure applied in Section 3, whereas Sections 4, 5, and 6 are devoted to method, results, and discussion, respectively. Finally, conclusions are given in Section 7.

2 DATA

The GIADA dust detector included three measurement subsystems: (a) the Grain Detection System (GDS), a laser curtain with photodiode sensors, measuring speed of individual dust particles within 0.3–100 m s^{-1} range; (b) the Impact Sensor (IS), a plate connected to piezoelectric sensors, measuring the momentum of individual dust particles, with a sensitivity of 10^{-10} kg m s^{-1}; and (c) the MicroBalance System (MBS), five quartz crystal microbalances facing in different directions, measuring the cumulative mass dust flux, with a sensitivity of 1.56 ng cm^{-2}. For dust particles detected by both GDS and IS units (i.e. GDS+IS detections) the mass can be determined from the momentum to speed ratio.

In this work, we considered all the detections of individual particles, i.e. events recorded by GDS, IS, or by both sensors (GDS+IS). Some dust particles were detected twice: (a) in the case of simultaneous GDS and GDS+IS measurements, we adopted the particle speeds from the GDS+IS measurement due to the increased accuracy; (b) in the case of two simultaneous detections from each of the two GDS scattered light detectors, we adopted the average of the two measurements. Thus, the total GIADA data set that we analysed here includes 5445 detections.

In order to study the temporal variation of dust ejection, we defined six periods, corresponding to the different orbital stages of comet 67P and characterized by different altitudes of the *Rosetta* spacecraft above the surface. The periods' definition is the same as the one proposed by Della Corte et al. (2016a) and is summarized in Table 1, together with the number of GIADA individual particles detected during each period.

3 TOOLS

Our traceback procedure took in consideration the dust particles' speed, directly measured in the case of GDS and GDS+IS detections, and retrieved from the following empirical relation (Della Corte et al.2016a) in the case of IS detections:

$$v = Am^{\gamma},$$

where v is the particle speed, A and γ are parameters depending on the heliocentric distance and the phase angle (in particular, γ is about -0.25 and -0.50 for phase angles smaller and larger than 75°, respectively), and $m = p/v$ is the particle mass, with p being the momentum directly measured by IS.

A specific analysis was made for dust showers. Dust showers are ensembles of GDS detections clustered in time, i.e. characterized by a detection frequency larger than 1 Hz, which are likely produced during the fragmentation of a single fluffy aggregate entering the spacecraft electrostatic potential (Fulle et al. 2015). In order to obtain the speed of the original fluffy particle generating the shower, we applied the method devised by Longobardo et al. (2019a), which we briefly describe in the following: (a) if the shower included a GDS+IS detection, its speed was assumed to be the fluffy particle's speed; (b) otherwise, a speed histogram was built and the most frequent value in the shower was assumed to be the fluffy particle's speed.

The discrimination process between fluffy and compact particles was based on the calibration activity performed with comet analogues (Della Corte et al. 2016b) and dust modelling (Fulle et al. 2015), which allowed to associate all the GDS+IS, IS, and isolated GDS detections (i.e. not grouped in dust showers) to compact particles and all the dust showers to fluffy aggregates.

Downloaded from https://academic.oup.com/mnras/article/496/1/125/5849013 by guest on 31 January 2025

Table 1. Definition of 67P/Churyumov–Gerasimenko's orbital stages and corresponding observation dates, distance comet–Sun, spacecraft altitude over the comet surface, and total number of individual GIADA detections (i.e. GDS, IS, and GDS+IS). Multiple detections associated with the same particle are counted only once. In the 2 weeks gap between Periods 1 and 2 there are no GIADA detections.

Period	Orbital stage	Start date (dd-mm-yy)	End date (dd-mm-yy)	Heliocentric distance (au)	Spacecraft altitude range (km)	No. of dust particles detected
0	First inbound arc	01-08-14	21-01-15	3.6–2.5	6–40	785
1	Second inbound arc	22-01-15	31-03-15	2.5–2.0	10–50	784
2	Pre-perihelion	14-04-15	30-06-15	1.9–1.4	120–180	373
3	Perihelion	01-07-15	31-10-15	1.3–1.6	180–500	751
4	First post-perihelion	01-11-15	22-02-16	1.6–2.4	100–500	1136
5	Second post-perihelion	23-02-16	15-09-16	2.4–3.8	0–18	1436

In order to correlate the dust particles detected to the surface morphology, we adopted the geomorphological classification proposed by El-Maarry et al. (2015, 2016). In fact, following their description of geomorphological regions, we discriminated between rough and smooth terrains. Specifically, we considered the Aker, Anhur, Ash, Atum, Bes, Geb, Khephry, Seth, Anuket, Bastet, Hathor, Maftet, Neith, and Sobeck regions 'rough' and the Anubis, Apis, Aten, Imhotep, Hatmeith, Ma'at, Nut, Wosret, and Hapi regions 'smooth'. Since the Babi, Khonsu, and Serqet regions present both rough and smooth terrains, they were classified as 'mixed'. However, such mixed terrains will not be taken into account when studying the link of dust ejection with the surface morphology. According to El-Maarry et al. (2016), one perihelion passage does not modify the large-scale morphology, therefore, we assumed that geomorphological regions maintain their character (rough/smooth/mixed) after the perihelion.

4 METHOD

In order to reconstruct the dust particles' motion back to the surface, we assumed a radial trajectory (in a non-rotating frame) from the comet nucleus to GIADA. The accuracy of this assumption depends on the spacecraft altitude above the comet's surface and the extent of its validity will be discussed for each mission stage. Based on coma dust models (e.g. Ivanovski et al. 2017), we assumed that the motion is uniformly accelerated up to an altitude of 11 km and then rectilinearly uniform (Zakharov et al. 2018).

From the particles' velocity and the spacecraft altitude, we derived the time of flight from the nucleus surface to GIADA for each dust particle, and, by accounting for the comet rotation, we identified its geomorphological region of ejection (details in Longobardo et al. 2019a).

Thus, we compared for each period (as defined in Table 1) the distribution of fluffy and compact particles in the coma and on the surface of the nucleus. This was done by relating the number of detected fluffy and compact particles per unit area in each geomorphological region, both before (i.e. in the coma) and after (i.e. on the nucleus) the application of the traceback procedure. For the before-traceback case, we referred to the coordinates of the detection in the coma as projected onto the surface. We considered the number of particles per unit area because larger regions obviously emit a larger number of particles, leading to a non-reliable correlation between the two dust populations.

We evaluated the correlation between ejection of fluffy and compact particles by means of the Pearson coefficient (already used for previous planetary science studies; e.g. Longobardo et al. 2019b), defined as $\sigma_{FC}/\sigma_F\sigma_C$, being σ_F and σ_C the variance of the number of fluffy and compact particles per unit area, respectively, and σ_{FC} their covariance. The Pearson coefficient value indicates the correlation degree: strong if larger than 0.7, moderate if in between 0.4 and 0.7, absent if smaller than 0.4. Negative coefficients indicate strong (i.e. between -0.7 and -1) to absent (i.e. between -0.4 and 0) anticorrelation.

Finally, we calculated for each period the fraction of fluffy and compact particles ejected by rough and smooth terrains, respectively.

The interpretation of the results obtained in this work was supported by thermal modelling, based on a 3D finite element method (FEM) scheme. The model solves a modified version of the classical heat equation, in which terms linked to the water vapour emission are present: no internal source or thermal convection is included (see e.g. Formisano et al. 2018, 2019a,b; Rinaldi et al. 2019). We simulated the comet surface temperature's temporal behaviour (integration domain is $1 \times 1 \times 5$ cm^3) at different heliocentric distances, representative of the periods listed in Table 1: 1.30 au (beginning of Period 3), 2.00 au (beginning of Period 2 and half of Period 4), 2.50 au (beginning of Periods 1 and 5), 3.30 au (beginning of the mission), and 3.80 au (end of the mission). The domain surface is generated by a random function, simulating the local topography. On the top of the domain a radiation boundary condition is imposed, while fixed temperatures are applied to the other sides. The following parameters were assumed: dust-to-ice ratio = 10 (an average value between literature estimates; e.g. Rotundi et al. 2015; Fulle et al. 2016, 2020; Cambianica et al. 2020), thermal inertia = 18 thermal inertia unit (TIU) compatible with a thermal conductivity of the order of 10^{-3}. Two different surface emissivity values (0.6 and 0.97) were assumed in order to simulate a rough and a smooth terrain, respectively. The albedo used is 0.05 (Shi et al. 2016).

5 RESULTS

The latitude and the longitude of the source dust regions obtained by our traceback procedure are affected by an uncertainty deriving from the propagation of the error $\Delta\upsilon$ on the measured speed (given by GIADA measurements, and ranging from 1 to 6 per cent of the velocity) to the time of flight. We quantified the subsolar point

Downloaded from https://academic.oup.com/mnras/article/496/1/125/5849013 by guest on 31 January 2025

latitude and longitude variations during the time Δt (Δt is the time of flight uncertainty) and adopted them as uncertainties on the retrieved coordinates of the ejecting regions: they obviously increase with h, i.e. depend on the periods defined in Table 1. As the subsolar latitude is poorly affected by rotation during short time-scales, the uncertainty on latitude is always negligible. On the contrary, the error bar on the derived longitude (i.e. two times the uncertainty) is on average 1.°6 for Period 0, 3.°6 for Period 1, 10° for Period 2, 22° for Period 3, 20° for Period 4, and 1.°2 for Period 5. Generally, the error bars are entirely included inside geomorphological regions, i.e. they are smaller than the geomorphological region longitude width. The number of 'doubtful' detections, i.e. the detections where the derived longitude error bar covers two or more geomorphological regions, will be presented for each analysed period. Since the fraction of doubtful detections are generally low, we do not show error bars on the number of particles ejected from each geomorphological region.

Figs 1–6 show the correlation between fluffy versus compact particles per unit area in the coma (i.e. as detected by GIADA) and on the nucleus (i.e. after the application of the traceback procedure) for the Periods 0–5, respectively.

In Period 0 (Fig. 1), the distributions of fluffy and compact particles are not correlated in the coma (Pearson coefficient is 0.2) but are correlated on the nucleus (Pearson coefficient is 0.7). Note that there are only three doubtful detections in this period (less than 1 per cent of the total GIADA detections). Thus, they cannot account for the different trends found.

The results of Period 1 are somewhat analogous (Fig. 2), with Pearson coefficient of 0.1 in the coma and of 0.7 on the surface. There are three doubtful detections in this case too (less than 1 per cent).

For the Period 2 there is no correlation between the distribution of dust and fluffy particles, neither in the coma (Pearson coefficient of 0.1) nor on the surface of the nucleus (Pearson coefficient of −0.1), as shown in Fig. 3. There are 26 doubtful detections in this period, which account for 15 per cent of the total detections.

The lack of a correlation between fluffy and compact particles distributions is also observed for Period 3, where the Pearson coefficients are 0.1 for both coma and nucleus (Fig. 4). Because of the highest spacecraft altitude, this is the period with most doubtful detections, 132, corresponding to 25 per cent of total number of detections.

Results are similar for Period 4 (Fig. 5), with Pearson coefficient of −0.1 in the coma and 0.1 on the nucleus and 64 doubtful detections (10 per cent of the total).

Finally, correlation is found in Period 5 both before and after the application of the traceback procedure, with Pearson coefficients of 0.8 and 0.9, respectively (Fig. 6). This period is characterized by the lowest spacecraft altitude on the surface and includes three doubtful detections.

Then, we calculated the overall fraction of fluffy and compact particles ejected from rough and smooth regions (as defined in Section 3) for Periods 0, 1, and 5 (the other periods were discarded from this analysis as will be explained in Section 6.2). The uncertainty associated with these fractions was obtained by propagating the uncertainties on the number of detected fluffy and compact particles, which are assumed to be Poissonian. The obtained results are summarized in Table 2.

In the data in Table 2, we find that the minimum ejection of fluffy particles is reached when approaching perihelion (i.e. Period 1) for smooth terrains, and after the perihelion for rough terrains.

6 DISCUSSION

6.1 Fluffy versus compact particles

We confirmed for Period 0 the results found by Longobardo et al. (2019a). The distributions of fluffy and compact dust particles are correlated on the nucleus but not in the coma: the two dust populations are ejected together and they are spread later on in the coma due to their different speeds. These results also apply to Period 1, i.e. until 2015 March 31.

In Periods 2–4 the distributions of fluffy and compact particles are not correlated on the nucleus either. However, this result is unreliable, because our simplistic traceback procedure cannot be applied to high spacecraft altitudes reached in these periods. This is due to the three reasons.

(i) The uncertainty on the ejecting region coordinates (and consequently the number of doubtful detections) increases with altitude. The doubtful detections fraction are between 10 and 25 per cent for Periods 2, 3, and 4, while it is less than 1 per cent for the other periods. Therefore, results obtained for these periods are more questionable.

(ii) According to numerical models (e.g. Zakharov et al. 2018), the motion of dust particles is no longer linear at altitudes higher than ∼40 km. This is also due to the solar radiation pressure, which deviates fluffy particles more efficiently with respect to compact ones (because of their larger cross-section-to-mass ratio). Therefore, the radial motion assumption cannot be applied during these periods, which are characterized by a spacecraft altitude from 100 to 400 km.

(iii) The low number of detected fluffy particles (zero in several regions) does not allow us to constrain a possible correlation between the two dust populations. This is due to deviation from radial motion, but probably also due to the low absolute values of the dust potential reached in these periods (Odelstad et al. 2017), which is not sufficient to disrupt fluffy aggregates into the showers detectable by GIADA.

For the reasons above, the Periods 2–4 were discarded and no longer considered for our analysis.

Period 5 shows a behaviour opposite to Periods 2–4: the fluffy and compact dust populations are correlated both before and after the application of the traceback method. This result is ascribed again to the spacecraft–comet distance, which was very low at this stage, i.e. on average 9 km (Table 1), and does not allow the spatial separation of the two populations due to short transit times.

This work therefore extends the results obtained by Longobardo et al. (2019a) for the first Churyumov–Gerasimenko inbound arc to the entire orbital stage observed during the *Rosetta* mission, i.e. fluffy and compact particles are contemporarily ejected from the nucleus surface and then spread in the coma, with a spatial separation of the two populations occurring at altitudes typically larger than 10 km.

6.2 Rough versus smooth terrains

Recent theoretical models (Fulle et al. 2020) have shown that, due to water-driven activity, most of dust particles are ejected from a depth depending on the surface temperature: this is between 10 μm and 2 cm when the comet is close to perihelion and its surface is hotter (temperature of 300 K), and between 1 mm and 6 cm when the comet is farther from the Sun and its surface is colder (temperature of 220 K). In fact, a larger

Downloaded from https://academic.oup.com/mnras/article/496/1/125/5849013 by guest on 31 January 2025

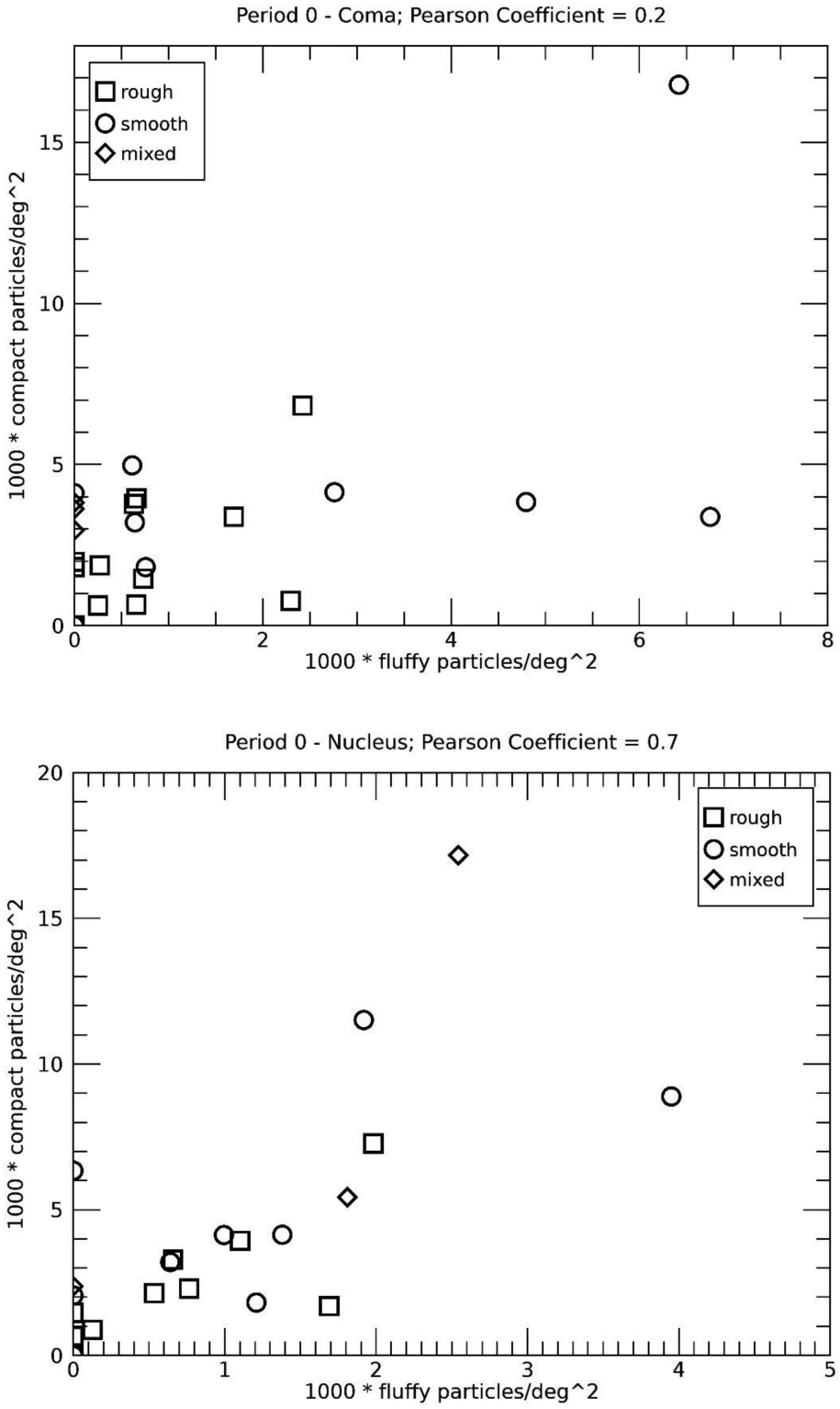

Figure 1. Correlation between the number of fluffy versus compact particles detected per unit area (in deg^2) by GIADA in Period 0 before (i.e. in the coma, top) and after (i.e. on the nucleus surface, bottom) the traceback procedure, respectively. Symbols are associated with geomorphological regions on which the detection coordinates are projected (coma case, top) and with geomorphological regions ejecting the dust particles (nucleus case, bottom), respectively. Squares, circles, and diamonds indicate rough, smooth, and mixed terrains. Pearson coefficients are 0.2 (top) and 0.7 (bottom).

Downloaded from https://academic.oup.com/mnras/article/496/1/125/5849013 by guest on 31 January 2025

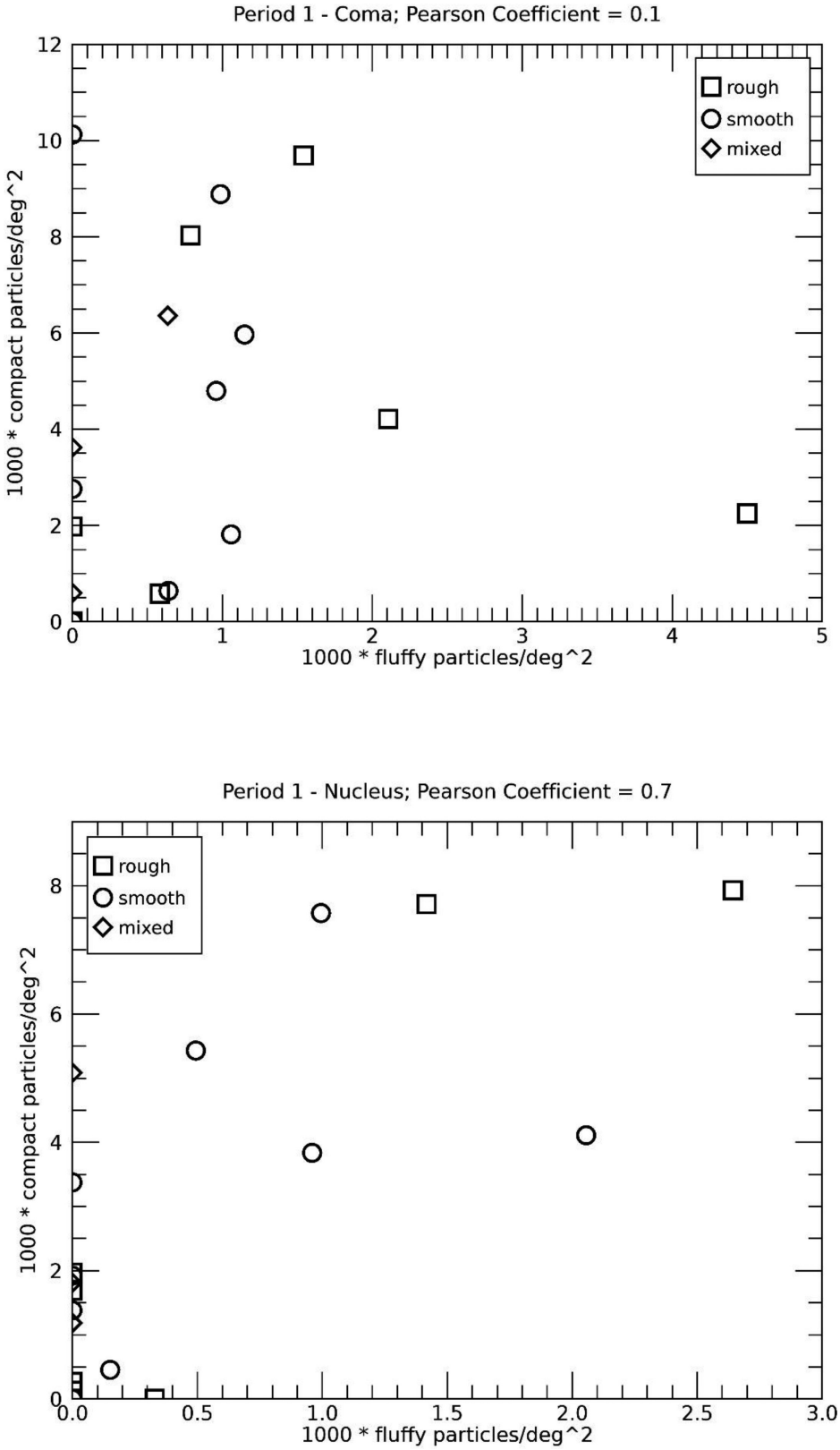

Figure 2. Same as Fig. 1, but for Period 1. Pearson coefficients are 0.1 (top) and 0.7 (bottom).

Downloaded from https://academic.oup.com/mnras/article/496/1/125/5849013 by guest on 31 January 2025

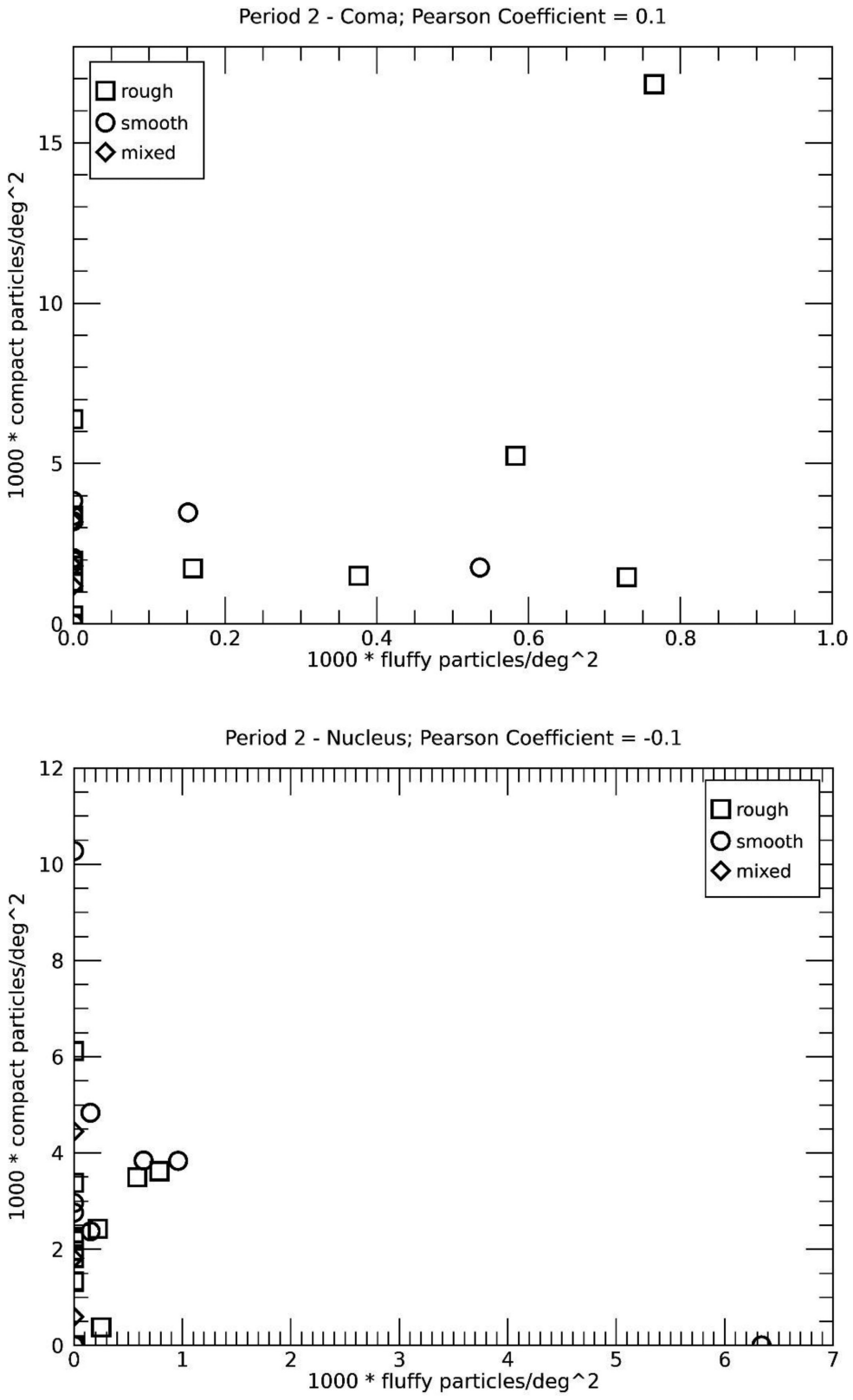

Figure 3. Same as Fig. 1, but for Period 2. Pearson coefficients are 0.1 (top) and −0.1 (bottom).

Downloaded from https://academic.oup.com/mnras/article/496/1/125/5849013 by guest on 31 January 2025

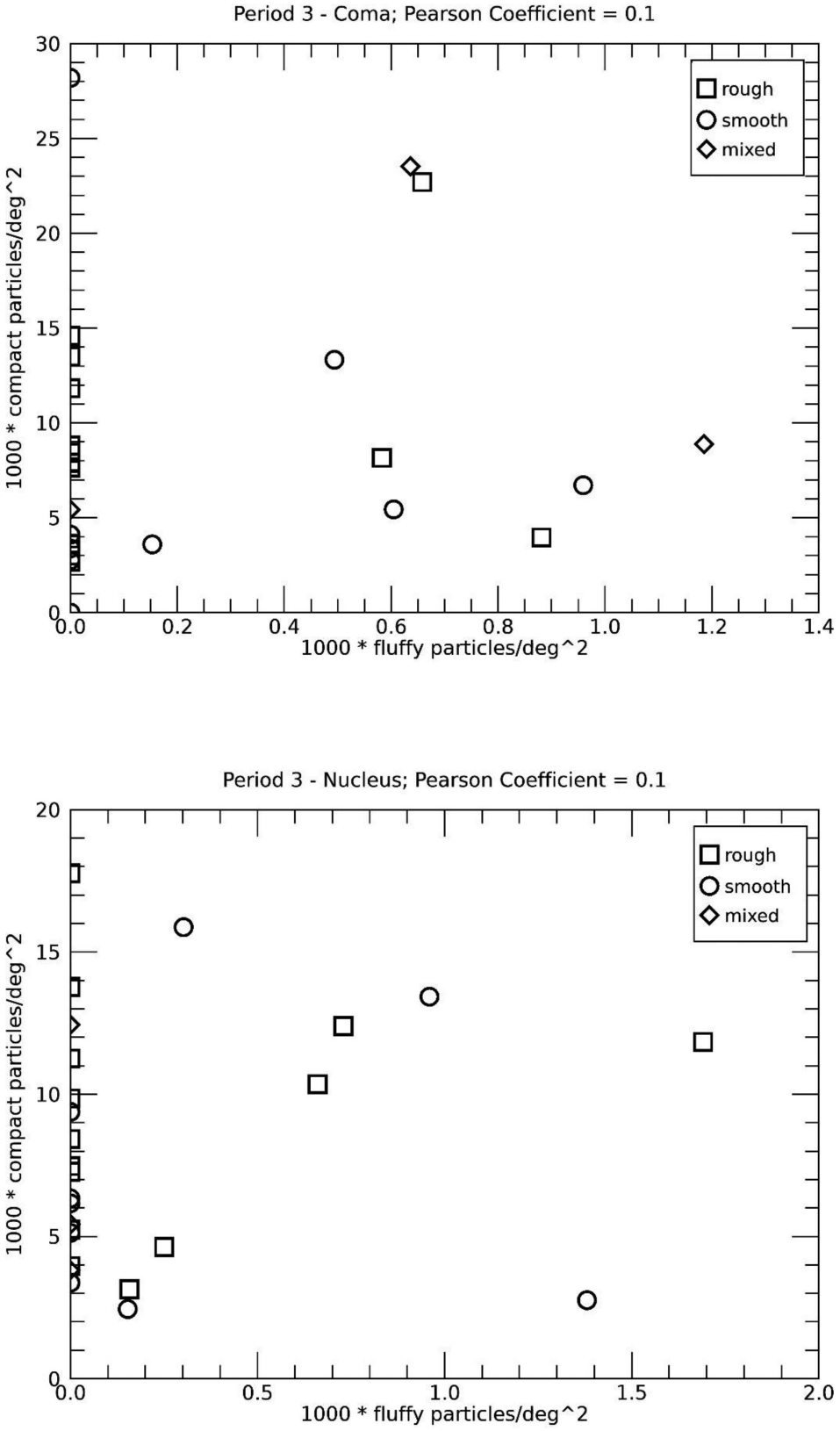

Figure 4. Same as Fig. 1, but for Period 3. Pearson coefficient is 0.1 in both cases.

Downloaded from https://academic.oup.com/mnras/article/496/1/125/5849013 by guest on 31 January 2025

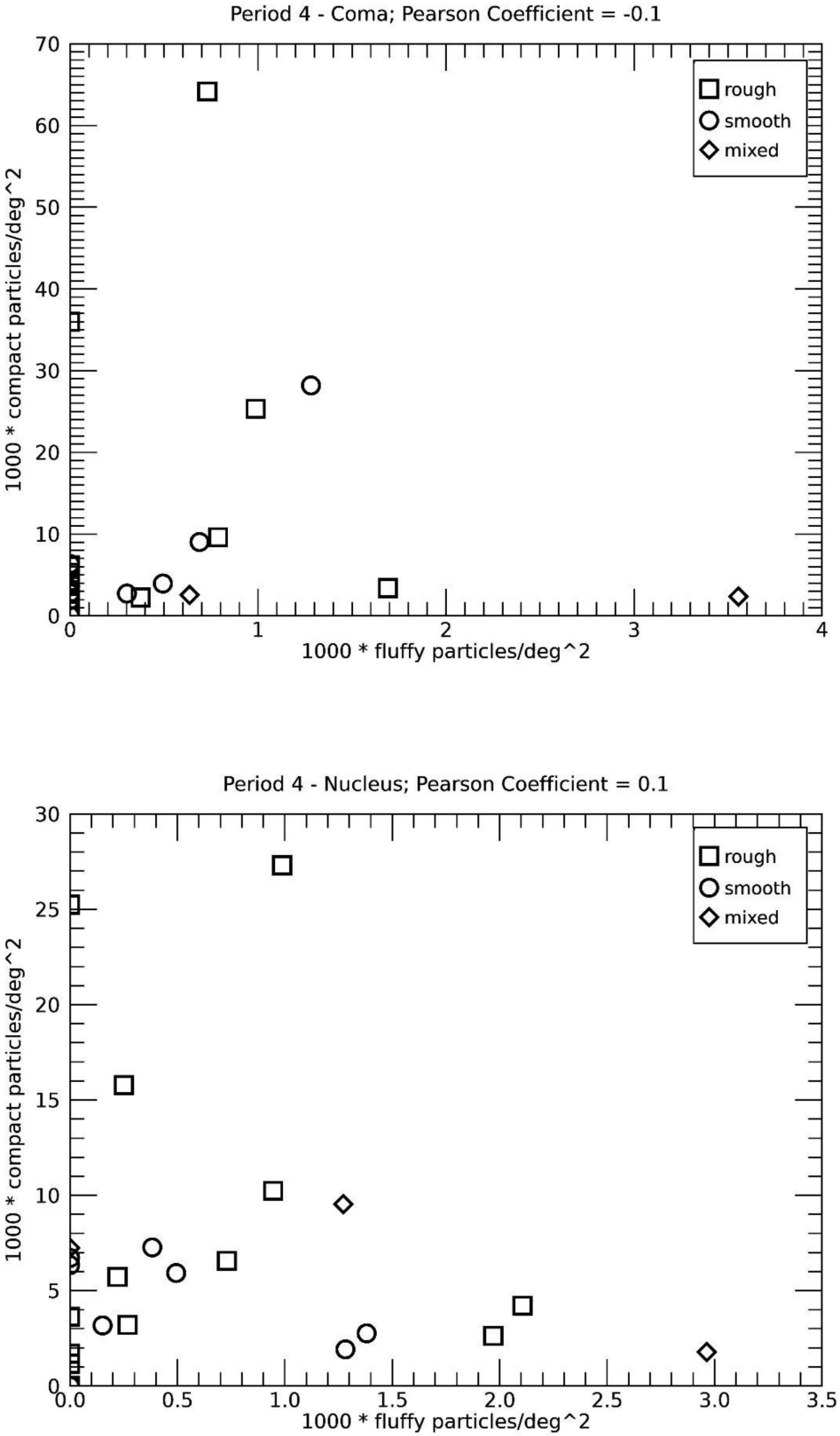

Figure 5. Same as Fig. 1, but for Period 4. Pearson coefficients are −0.1 (top) and 0.1 (bottom).

Downloaded from https://academic.oup.com/mnras/article/496/1/125/5849013 by guest on 31 January 2025

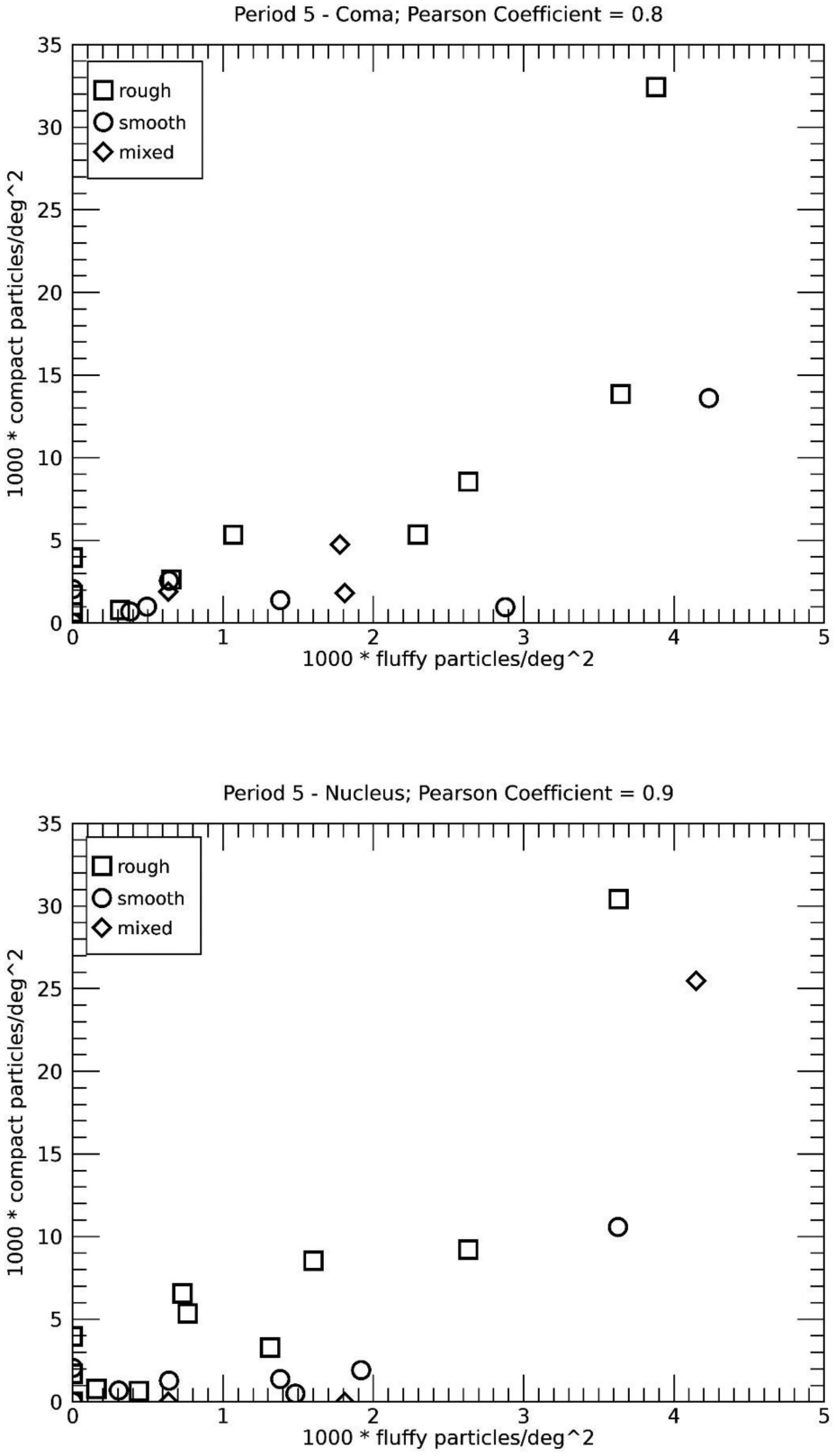

Figure 6. Same as Fig. 1, but for Period 5. Pearson coefficients are 0.8 (top) and 0.9 (bottom).

Downloaded from https://academic.oup.com/mnras/article/496/1/125/5849013 by guest on 31 January 2025

Table 2. Percentage of fluffy particles ejected from all the Churyumov–Gerasimenko's rough and smooth terrains, respectively, in Periods 0, 1, and 5. The percentage of compact particles is complementary (100 minus the values given in the table).

	Percentage of fluffy particles			
	Period 0	Period 1		Period 5
Rough terrains	25 ± 4	21 ± 4	Perihelion	14 ± 2
Smooth terrains	24 ± 4	12 ± 3		29 ± 5

surface temperature is associated with a steeper thermal gradient and therefore probes shallower depths. Because fluffy particles reside at surface depths larger than 1 cm (Fulle & Blum 2017), we should expect an increasing fraction of ejected compact particles, i.e. a minimum of fluffy particles abundance, when approaching perihelion. However, this behaviour is observed only in smooth terrains, whereas in rough terrains the smallest fraction of fluffy particles are reached after perihelion (Table 2). We studied the impact of surface thermal properties and of dust redeposition on this result.

6.2.1 *Surface's thermal properties*

We started our analysis by assuming that thermal properties of rough terrains could delay the temperature peak that could explain why for the rough terrains we registered more compact particles after perihelion in comparison with smooth terrains. In order to verify this hypothesis, we simulated the thermal behaviour of a rough and smooth terrain by applying the thermal model described in Section 4. The roughness was simulated by considering two different emissivity values, i.e. 0.6 for rough terrain and 0.97 for smooth terrain. In fact, due to self-heating, an increasing roughness leads to a re-emitted radiation (emissivity) decrease and a temperature increase (e.g. Davidsson, Gutiérrez & Rickman 2009). The considered emissivity difference between rough and smooth terrains is much larger than the emissivity spread expected on comet 67P/Churyumov–Gerasimenko's surface (e.g. Spohn et al. 2015), and consequently the simulated temperature difference between rough and smooth terrains is also larger than the one measured (that is of a few degrees; see Tosi et al. 2019). However, we were only interested into finding a possible relation between temperature behaviour and surface roughness. Simulations were performed for five different heliocentric distances, covering the six periods (the 2.0 and 2.5 au heliocentric distances correspond to two periods each, before and after perihelion, respectively). For each heliocentric distance, the maximum temperature reached was considered (i.e. the daily peak temperature).

Fig. 7 shows the simulated daily peak temperature behaviour in the rough and smooth terrains throughout the entire *Rosetta* mission. Apart from the values (also depending on the assumed thermal gradient), obviously larger in the rough terrain, the temporal behaviour is the same in the two terrains and there is no delay in the reaching peak temperature between rough and smooth terrains.

Previous works (Marshall et al. 2018) have suggested that thermal inertia, which affects the temporal temperature behaviour, is also independent of surface roughness.

We conclude that the surface temperature's temporal behaviour alone cannot explain the observed differences in compact versus fluffy dust ejection and that surface's intrinsic thermal properties do not affect the observed behaviour.

6.2.2 *Dust fallback*

Then we considered the possible impact of dust fallback on the comet surface (e.g. Kramer & Noack 2015; Hu et al. 2017; Keller et al. 2017a) on the results in Table 2 to relate dust porosity and surface geomorphology. In fact, dust could be transferred among comet regions via ejection and following redeposition: when re-ejected, it does not carry information from the ejecting region.

Therefore, the study of dust properties in rough and smooth terrains requires the discrimination between the dust directly emitted from the comet (i.e. sampling the region of origin) and the dust previously ejected, fallen back, and then re-ejected. Based on previous results (Schulz et al. 2015; Pajola et al. 2017), we can consider 3.0 au as threshold separating the two kinds of ejection. Roughly, we assumed that ejection at heliocentric distances larger than the threshold is dominated by dust particles not originating but previously deposited on the emitting region, while direct emission is dominant at closer distances.

Under this assumption, we adopted a new definition of the orbital stages listed in Table 1. In the Period 0, we separated orbital distances larger and lower than 3 au, respectively. All the detections occurred outside 3 au were grouped in the new Period A. The new Period B includes the Period 0 detections at distances lower than 3 au and all the Period 1 detections. Finally, the Period C coincides with the post-perihelion Period 5. In Period 5 we did not separate the orbital distances larger and lower than 3 au, as done for Period 0, for two reasons: (a) the number of detections at distances lower than 3 au is too low for statistically significant results; (b) this period followed the dust activity peak, and therefore the dust fallback might already be significative compared to the direct ejection of dust. The new orbital stages definition is summarized in Table 3.

To infer the fluffy and compact particles abundance difference between rough and smooth terrains, we calculated the abundance variations with respect to Period A. In other words, we calculated for both rough and smooth terrains the fluffy (and compact) particle fraction difference relative to Period A (for the Period A, this difference is obviously zero). In fact, Period A is not representative of direct dust ejection and is just considered as reference for the other two periods. In this sense, information about the occurrence of fluffy and compact particles in rough and smooth terrains is given from their fractional variation from Period A to Period B. In Period C, we should observe a negligible variation with respect to Period A, because the two dust populations are mixed again because of fallback following the cometary peak activity. The obtained results are reported in Table 4 for fluffy particles (results of compact particles are the same but with the opposite sign). The uncertainties were calculated by propagating the errors of the fluffy particle fractions by means of summation in quadrature.

In the Period B, the fluffy particle variation is negative for smooth terrains and positive for rough terrains. In the Period C, the variation is consistent with zero, as expected.

This indicates that, during cometary phases of direct emission, fluffy particles were more abundant in rough terrains and compact particles were more abundant in smooth terrains, indicating a correspondence between the most primitive dust particles (the fluffy ones) and the less processed terrains (the rough ones). We identified two possible explanations for this behaviour.

(i) Smooth terrains have been more modelled by dust activity during the earlier perihelion passage(s). Specifically, their smooth appearance is also due to deposits of ejected and then fallen back dust (e.g. El-Maarry et al. 2015). This dust is mainly composed of compact particles (Fulle et al. 2020).

Downloaded from https://academic.oup.com/mnras/article/496/1/125/5849013 by guest on 31 January 2025

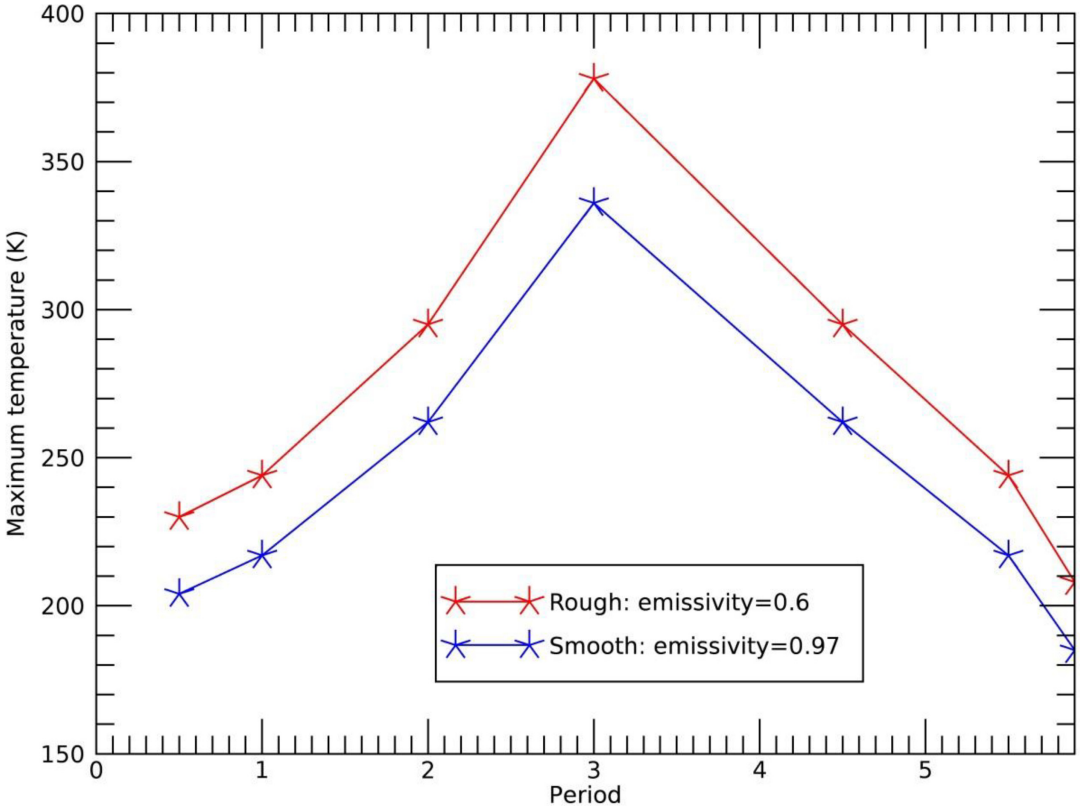

Figure 7. Modelled temporal behaviour of the maximum diurnal temperature reached in a rough (emissivity = 0.6) and a smooth (emissivity = 0.97) comet terrain. The *x*-axis reports the Period as defined in Table 1. The seven asterisks correspond to the following orbital distances (in au): 3.3, 2.5, 2.0, 1.3 (perihelion), 2.0, 2.5, and 3.8.

Table 3. Definition of 67P/Churyumov–Gerasimenko's orbital stages adopted to take into account the dust fallback. The third column relates this definition with that adopted in Table 1. The Periods 2, 3, and 4 defined in Table 1 are not considered in this analysis, because of poorly reliable results.

Period	Orbital distance (au)	Corresponding to
A	3.6–3.0	First part of Period 0
B	3.0–2.0	Second part of Period 0+Period 1
	Perihelion	
C	2.4–3.8	Period 5

Table 4. Fluffy particle fraction variation with respect to the Period A in rough and smooth terrains. Uncertainties are calculated by means of summation in quadrature. The variations of compact particles fraction are the opposite of the values reported in the table.

	Percentage of fluffy particles			
	Period A	Period B		Period C
Rough terrains	0	9 ± 5	Perihelion	-2 ± 4
Smooth terrains	0	-14 ± 4		1 ± 5

(ii) Fluffy particles are stored between the voids among the cm-sized pebbles randomly packed on the comet surface. Boulder size distributions have shown a distribution peak at about 20 cm ('chunks') in smooth terrains (Mottola et al. 2015; Pajola et al. 2017), a size much larger than pebbles. This implies that smooth terrains have two macroporosity levels: (a) among pebbles and rough terrains, i.e. voids filled with fluffy particles (Fulle & Blum 2017) and (b) among 'chunks', which are typical of smooth terrains and not present in rough terrains, and which cannot be filled by fluffy particles, because these voids are not pristine, being created during the fallout. According to comet formation models (Fulle & Blum 2017; Blum et al. 2017), this second level of porosity decreases the volume available to fluffy particles of 37 ± 5 per cent, i.e. the volume filling factor of random packing of spheres. Our results show that the fluffy particles amount variation between rough and smooth terrains is 23 ± 9 per cent (given by the difference of the two values reported in the 'Period B' column in Table 4), which agrees with the model prediction within the error.

7 CONCLUSIONS

We extended the procedure to trace back Churyumov–Gerasimenko's coma dust particles down to the nucleus surface from the first inbound arc (Longobardo et al. 2019a) to the entire orbit arc observed by the *Rosetta* mission.

We confirmed that in the first mission period (end of 2014 and 2015 January) fluffy and compact dust particles were ejected contemporarily from common nucleus surface areas and then were spread during the motion due to their different ejection speeds. This result is valid also for the second inbound arc (2015 January) and for the post-perihelion stage (2016). The separation between the two dust populations is observed at surface altitudes higher than 10 km, because at this distance the spatial distributions of fluffy and compact dust particles are still correlated. Our traceback procedure is instead not reliable for the orbital stages close to

Downloaded from https://academic.oup.com/mnras/article/496/1/125/5849013 by guest on 31 January 2025

perihelion, because its simplistic assumptions are not valid at the high spacecraft altitudes (i.e. >100 km) reached in these periods. In this case, numerical models including all the different processes acting on a dust particle's motion will be necessary to trace back the dust.

We studied the distribution of fluffy and compact dust particles in the rough and smooth comet regions, finding that fluffy particles concentration is about 25 per cent larger in the rough terrains. This is in agreement with the lower resurfacing of rough terrains by deposition of compact particles ejected by past water-driven activity. It is also in agreement with the larger concentration in rough terrains of cm-sized pebbles, able to store fluffy particles among them. The retrieved variation of fluffy particles between rough and smooth terrains agrees with the predictions from up-to-date comet formation and evolution models (e.g. Fulle et al. 2020).

ACKNOWLEDGEMENTS

This research was supported by the Italian Space Agency (ASI) within the ASI-INAF agreement I/032/05/0 and by the International Space Science Institute (ISSI) through the ISSI International Team 'Characterization of cometary activity of 67P/Churyumov–Gerasimenko comet'.

GIADA was built by a consortium led by the Universitá degli Studi di Napoli 'Parthenope' and INAF – Osservatorio Astronomico di Capodimonte, in collaboration with the Instituto de Astrofisica de Andalucia, Selex-ES, FI, and SENER. GIADA is presently managed and operated by Istituto di Astrofisica e Planetologia Spaziali-INAF, Italy. GIADA was funded and managed by the Agenzia Spaziale Italiana, with the support of the Spanish Ministry of Education and Science Ministerio de Educacion y Ciencias (MEC). GIADA was developed from a Principal Investigator proposal from the University of Kent; science and technology contributions were provided by CISAS, Italy, Laboratoire d'Astrophysique Spatiale, France, and institutions from the UK, Italy, France, Germany, and the USA. Science support was provided by NASA through the U.S. *Rosetta* Project managed by the Jet Propulsion Laboratory/California Institute of Technology. We would like to thank A. Coradini for her contribution as a GIADA Co-Investigator. GIADA calibrated data are available through ESA's Planetary Science Archive (PSA) website (http://www.rssd.esa.int/index.php?project = PSA&page = index).

The work has benefited of discussions with INAF-IAPS researchers (Gianrico Filacchione, Fabrizio Oliva, and Federico Tosi).

TM acknowledges funding by the Austrian Science Fund FWF P 28100-N36.

REFERENCES

Barucci M. A. et al., 2016, A&A, 595, A102
Blum J. et al., 2017, MNRAS, 469, S755
Bockelée-Morvan D. et al., 2017, MNRAS, 469, S443
Cambianica P. et al., 2020, A&A, 636, A91
Capaccioni F. et al., 2015, Science, 347, aaa0628
Ciarniello M. et al., 2016, MNRAS, 462, S443
Coradini A. et al., 2007, Space Sci. Rev., 128, 529
Davidsson B. J. R., Gutiérrez P. J., Rickman H., 2009, Icarus, 201, 335
Della Corte V. et al., 2014, J. Astron. Instrum., 3, 1350011
Della Corte V. et al., 2016a, MNRAS, 462, S210
Della Corte V. et al., 2016b, Acta Astronautica, 126, 205
Della Corte V. et al., 2019, A&A, 630, A25
De Sanctis M. C. et al., 2015, Nature, 525, 500
El-Maarry M. R. et al., 2015, A&A, 583, A26
El-Maarry M. R. et al., 2016, A&A, 593, A110
Filacchione G. et al., 2016, Nature, 529, 368
Formisano M., Federico C., De Sanctis M. C., Frigeri A., Magni G., Raponi A., Tosi F., 2018, J. Geophys. Res.: Planets, 123, 2445
Formisano M., De Sanctis M. C., De Angelis S., Carpenter J. D., Sefton-Nash E., 2019a, Planet. Space Sci., 169, 8
Formisano M., Federico C., Magni G., Raponi A., De Sanctis M. C., Frigeri A., 2019b, J. Geophys. Res.: Planets, 124, 2
Fulle M., Blum J., 2017, MNRAS, 469, S39
Fulle M. et al., 2015, ApJ, 802, L12
Fulle M. et al., 2016, ApJ, 821, 19
Fulle M., Blum J., Rotundi A., Gundlach B., Güttler C., Zakharov V., 2020, MNRAS, 493, 4039
Güttler C. et al., 2019, A&A, 630, A24
Hu X. et al., 2017, A&A, 604, A114
Ivanovski S. L., Zakharov V. V., Della Corte V., Crifo J.-F., Rotundi A., Fulle M., 2017, Icarus, 282, 333
Keller H. U. et al., 2007, Space Sci. Rev., 128, 433
Keller H. U. et al., 2017, MNRAS, 469, S357
Kramer T., Noack M. 2015, ApJ, 813, L33
Longobardo A. et al., 2019a, MNRAS, 483, 2165
Longobardo A. et al., 2019b, Icarus, 318, 241
Marshall D. et al., 2018, A&A, 616, A122
Merouane S. et al., 2017, MNRAS, 469, S459
Mottola S. et al., 2015, Science, 349, aab0232
Odelstad E., Stenberg-Wieser G., Wieser M., Eriksson A. I., Nilsson H., Johansson F. L., 2017, MNRAS, 469, S568
Pajola M. et al., 2017, MNRAS, 469, S636
Poch O. et al., 2020, Science, 367, eaaw7462
Raponi A. et al., 2016, MNRAS, 462, S476
Raponi A. et al., 2020, Nat. Astron., 4, 500
Rinaldi G. et al., 2016, MNRAS, 462, S547
Rinaldi G. et al., 2019, A&A, 630, A21
Rotundi A., the International GIADA Consortium, 2019, Rosetta-Orbiter 67P GIADA 5 Dust Maps V1.0, RO-C-GIA-5-67P-DUST-MAPS-V1.0. ESA Planetary Science Archive and NASA Planetary Data System
Rotundi A. et al., 2015, Science, 347, aaa3905
Schulz R. et al., 2015, Nature, 518, 216
Shi X. et al., 2016, A&A, 586, A7
Sierks H. et al., 2015, Science, 347, aaa1044
Spohn T. et al., 2015, Science, 349, aab0464
Tosi F. et al., 2019, Nat. Astron., 3, 649
Tubiana C. et al., 2019, A&A, 630, A23
Zakharov V. V., Ivanovski S. L., Crifo J.-F., Della Corte V., Rotundi A., Fulle M., 2018, Icarus, 312, 121

This paper has been typeset from a TEX/LATEX file prepared by the author.

Downloaded from https://academic.oup.com/mnras/article/496/1/125/5849013 by guest on 31 January 2025